

Phase Dynamics of Self-Accelerating Bose–Einstein Condensates

Maximilian L. D. D. Pellner¹ and Georgi Gary Rozenman²

¹Fakultät für Physik, Ludwig-Maximilians-Universität, München, Germany

²Department of Mathematics, Massachusetts Institute of Technology, Cambridge, Massachusetts 02139, USA

February 3, 2026

Self-accelerating Airy matter waves offer a clean setting to access the cubic Kennard phase. Here we reconstruct the relative phase of simulated Airy-shaped Bose–Einstein condensates in free space, a regime approached in microgravity, from interference fringes. The cubic phase dynamics are quantified via windowed polynomial fits with systematics-aware uncertainty estimates that account for window-induced correlations. We compare two experimentally feasible phase-extraction methods – heterodyne-based and density-based – and show that an Airy-Gaussian geometry yields substantially improved robustness to fit-window selection relative to an Airy-Airy collision. In the weakly interacting regime, the extracted cubic coefficient responds linearly to the effective one-dimensional interaction strength. Our approach turns cubic phase dynamics into a practical probe of weak mean-field nonlinearities in self-accelerating condensates.

1. INTRODUCTION

Since their first experimental realizations in dilute atomic gases in 1995 [1, 2], Bose–Einstein condensates (BECs) have emerged as a versatile platform for studying macroscopic quantum phenomena [3–6]. At ultracold temperatures, a large fraction of the atoms occupy a single quantum state, giving rise to coherence properties analogous to those of lasers in optics [7, 8]. This unique feature has made BECs a fertile ground for exploring fundamental questions in quantum mechanics, nonlinear wave dynamics [9], and analog models of condensed matter [10] and cosmology [11]. At the theoretical level, their mean-field dynamics are widely captured by the Gross–Pitaevskii equation, with driven–dissipative generalizations extending this framework to other quantum fluids such as exciton–polariton and photonic condensates [12, 13].

The vast majority of studies to date has focused on condensates prepared in ground states of harmonic traps, which are often well approximated by Gaussian-like profiles in the weakly interacting limit [3, 5]. Such simple ground states provide a natural starting point for investigating equilibrium properties, collective excitations, and nonlinear interactions. Upon release from the trap, the ensuing time-of-flight expansion of such states is well understood in terms of ballistic, essentially self-similar expansion, providing a standard baseline for interferometric and dynamical studies [7, 14, 15]. However, the restriction to near-Gaussian ground states limits the exploration of more exotic dynamics that can arise from nontrivial initial conditions [3, 5].

In parallel, structured wave packets beyond near-equilibrium ground states have attracted long-standing interest across quantum mechanics and wave physics. A particularly striking example is the Airy wave packet examined by M. V. Berry and N. L. Balazs, which is characterized by its unique dispersionless evolution maintaining its functional form, while its caustic follows a

parabolic trajectory even in the absence of an external force [16].

Because the ideal Airy solution carries infinite energy, physical realizations rely on finite-energy truncations. In optics these were introduced and experimentally observed as accelerating Airy beams [17, 18], which also exhibit self-healing after partial obstruction [19]. Airy-type wave packets have since been demonstrated in other diffractive and dispersive wave systems, including free-electron beams [20].

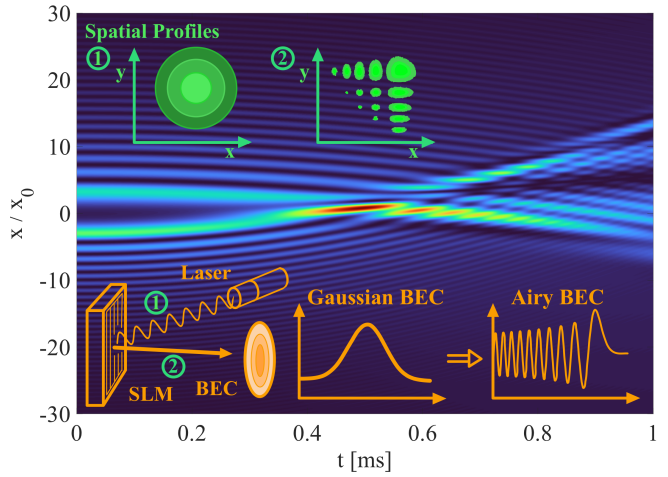


Figure 1. Time evolution of density $|\Psi(x, t)|^2$: Interference of two counterpropagating Airy-Bose-Einstein Condensates (Ai-BECs) in free space. A slightly asymmetric scenario of the Airy scales $x_{0,1}, x_{0,2} = 1.3 \cdot x_{0,1}$ is chosen, otherwise the cubic phase dynamics cancel out. Inset: Schematic of a possible experimental implementation in which an Airy-type, laser-induced potential by a spatial light modulator (SLM) is imprinted onto a Gaussian-like BEC ground state, producing an Ai-BEC.

Complementarily, wave packets of arbitrary shape evolving in a linear potential acquire a spatially uniform phase term that is cubic in time. This global cubic phase factor appears in the quantum-mechanical propagator of a particle subject to a constant force and was already

derived by E. H. Kennard in 1927 [21, 22]. It is commonly referred to as the Kennard phase [22, 23]. Airy wave packets also inherently exhibit cubic phase dynamics independent of the position, even in the absence of an external potential as already apparent in the Berry–Balazs solution [16]. This deep intrinsic connection between this property and the former quantum mechanical evolution is consistent with the fact that Airy functions are eigenstates of such linear potentials [24].

This Kennard phase has been observed in surface-gravity water waves, which provide a quantum-mechanical analog platform governed by a Schrödinger-type equation with an effective linear potential [23, 25, 26].

The same cubic-in-time phase term underpins T^3 matter-wave interferometry schemes based on state-dependent forces [22]. Recently, the Kennard phase was experimentally realized in an atom-chip-based Stern–Gerlach matter-wave interferometer [27]. In microgravity, a near-free-fall environment with well-characterized residual gradients provides a clean setting in which the following free-space interferometric collisions can, in principle, be implemented [28, 29].

These developments motivate exploring Airy-shaped initial states in ultracold quantum gases, where mean-field interactions provide a controlled nonlinearity and interference readout offers indirect access to the evolving phase. However, standard cold-atom imaging measures the density, and phase – especially spatially uniform terms – can only be accessed as a relative phase in an interferometer [7], making it sensitive to global and spatially varying phase drifts and to density-dependent mean-field phase accumulation [3, 5, 30]. Using the noninteracting evolution as a benchmark, the following simulations indicate that in the weakly interacting regime the cubic-in-time phase contribution varies approximately linearly with interaction strength in the perturbative range, while at larger interactions it departs from this trend and becomes distinctly nonlinear.

In this work, the interference of Airy-shaped BEC wave packets (Ai-BECs) is studied, yielding predictions for the intrinsic cubic phase dynamics in the weakly interacting regime. It is shown that interferometric data can be demodulated to isolate the spatially uniform cubic-in-time term, thereby enabling access to the Kennard phase as a relative phase in an interacting condensate setting. Based on simulations, two phase-reconstruction procedures – heterodyne-based and density-based – are proposed and benchmarked. Sensitivity to the choice of analysis window is quantified by scanning the fit interval, and uncertainties are estimated using heteroskedasticity and autocorrelation consistent Newey–West standard errors. Thus, the study provides theoretical guidance and simulation-based motivation for extending ultracold-gas interferometry beyond near-Gaussian initial states to self-accelerating, nearly non-

spreading and self-healing quantum-fluid matter waves over finite times [16, 18, 19].

2. THEORETICAL MODEL

The dynamics of a dilute Bose-Einstein condensate at ultracold temperatures is accurately described by the Gross–Pitaevskii equation (GPE), a nonlinear Schrödinger equation that incorporates mean-field interactions between the atoms [3, 5, 6],

$$i\hbar \frac{\partial \Psi(\mathbf{r}, t)}{\partial t} = \left[-\frac{\hbar^2}{2m} \nabla^2 + V(\mathbf{r}, t) + g_{3D} |\Psi(\mathbf{r}, t)|^2 \right] \Psi(\mathbf{r}, t), \quad (1)$$

where $\Psi(\mathbf{r}, t)$ is the condensate wavefunction normalized such that $\int |\Psi|^2 d\mathbf{r} = N$, with N the number of atoms. Here, m is the atomic mass, $V(\mathbf{r}, t)$ is an external potential, and $g_{3D} = 4\pi\hbar^2 a_s/m$ is the three-dimensional interaction strength with a_s the s-wave scattering length [3, 5].

In the weakly interacting regime, the dynamics are well captured at leading order by the linear Schrödinger equation, providing an analytic reference [3, 5]. In the simulations, the full time evolution is obtained with a split-step method. The residual interaction effects are included via the nonlinear phase shift $\Psi(x, t) \mapsto \exp[-i(g/\hbar)|\Psi(x, t)|^2 \Delta t] \Psi(x, t)$ with the normalization $\int |\Psi(x, t)|^2 dx = 1$ [31]. Unless stated otherwise, g denotes this effective one-dimensional control parameter used in the numerics. In what follows, for convenience, a quasi-one-dimensional condensate is considered [32], where the dynamics are effectively restricted to the x direction,

$$i\hbar \frac{\partial}{\partial t} \Psi(x, t) = \left[-\frac{\hbar^2}{2m} \frac{\partial^2}{\partial x^2} + V(x) \right] \Psi(x, t). \quad (2)$$

By choosing a linear potential $V = Fx$, and using the ansatz $\Psi(x, t) = \psi(x) e^{-i\mu t/\hbar}$ of the stationary eigenstates, the linear Schrödinger equation simplifies to the following equation with $l = \frac{\mu}{F}$:

$$\frac{d^2\psi}{dx^2} - \frac{2mF}{\hbar^2} (x - l) \psi(x) = 0. \quad (3)$$

Introducing the characteristic length scale $x_0 = \left(\frac{\hbar^2}{2mF}\right)^{1/3}$ and the dimensionless variables $\xi = \frac{x-l}{x_0}$ and $\tau = \frac{\hbar t}{m x_0^2}$ for the subsequent time propagation, one obtains the Airy equation [24]:

$$\frac{d^2\psi}{d\xi^2} - \xi \psi(\xi) = 0. \quad (4)$$

The corresponding Airy eigenstates are $\text{Ai}(\xi)$ and $\text{Bi}(\xi)$, of which the former is physically admissible, since $\text{Bi}(\xi)$ diverges for $\xi \rightarrow +\infty$ and is therefore not square-integrable [24, 33]. The profound Fourier representation

[16] is particularly relevant in the present context, as it reveals the rich structure of the nontrivial momentum distribution,

$$\text{Ai}(\xi) = \frac{1}{2\pi} \int_{-\infty}^{\infty} \exp\left[i\left(\frac{k^3}{3} + \xi k\right)\right] dk. \quad (5)$$

2.1. Single Airy Propagation and Phase Dynamics

In order to analytically derive the phase dynamics for $g = 0$, the Feynman propagator convolution is computed. The wave packet is evolved by evaluating

$$\Psi(\xi, \tau) = \int d\xi' K(\xi, \tau, \xi', 0) \psi(\xi') \quad (6)$$

as the integral of the wave packet itself multiplied by the Feynman propagator of free propagation

$$K(\xi, \tau; \xi', 0) = \frac{1}{\sqrt{2\pi i\tau}} \exp\left[\frac{i(\xi - \xi')^2}{2\tau}\right] \quad (7)$$

[34, 35]. For the experimental realization, the practical model is the exponentially truncated first Airy solution, which has finite energy [17] and therefore is physically meaningful and numerically computable,

$$\psi_{\text{Ai}}(\xi) = C \text{Ai}(\xi) e^{a\xi}, \quad a > 0. \quad (8)$$

After a few manipulations of the integral - in particular completing the square in the exponent, evaluating the Gaussian integral, performing a change of variables for a transverse shift and rewriting the result, Eq. (6) yields

$$\Psi_{\text{Ai}}(\xi, \tau) = C \exp\left[-\frac{a\tau^2}{2} + a\xi + i\left(-\frac{\tau^3}{12} + \frac{\tau\xi}{2} + \frac{a^2\tau}{2}\right)\right] \cdot \text{Ai}\left(\xi - \frac{\tau^2}{4} + i a \tau\right). \quad (9)$$

Finally, the relevant phase — including the Kennard phase, the characteristic cubic term in τ — can be extracted straightforwardly,

$$\Phi_{\text{Ai}}(\xi, \tau) = -\frac{\tau^3}{12} + \frac{\tau\xi}{2} + \frac{a^2\tau}{2}, \quad (10)$$

[17], where the imaginary component in the argument of the Airy function is neglected. Intuitively, for sufficiently large numerical simulation domains, the apodization parameter a can be chosen small enough that its influence on the phase dynamics becomes negligible. In the limit $a \rightarrow 0$, the contribution of the complex shift of the Airy argument vanishes entirely. For a rigorous discussion of the residual impact at small finite choices of a along the main lobe, see the supplementary analysis of Rozenman et al [23].

2.2. Single Gaussian Propagation and Phase Dynamics

Analogously to the previous calculation, the evolution of a stationary, i.e. zero-momentum, Gaussian wave packet

$$\Psi_{G,0}(\xi) = \frac{1}{(2\pi s^2)^{\frac{1}{4}}} \exp\left[-\frac{\xi^2}{4s^2}\right] \quad (11)$$

is obtained via convolution with the Feynman propagator, where $s = \frac{\sigma_0}{x_0}$ denotes the dimensionless normalized width at $t = 0$, and $\eta = \frac{\tau}{2s^2}$. Thereby, the resulting time-dependent general solution reads

$$\Psi_G(\xi, \tau) = \frac{1}{\left(2\pi (s\sqrt{1+i\eta})^2\right)^{\frac{1}{4}}} \cdot \exp\left[-\frac{\xi^2}{4(s\sqrt{1+i\eta})^2}\right]. \quad (12)$$

The effective time-dependent normalized width is given by $s_c(\tau) = s\sqrt{1+i\eta}$. Furthermore, Eq. 12 can be transformed into

$$\Psi_G(\xi, \tau) = \frac{1}{\left(2\pi (s\sqrt{1+\eta^2})^2\right)^{\frac{1}{4}}} \cdot \exp\left[i\left(\frac{\eta\xi^2}{4s^2(1+\eta^2)} - \frac{1}{2}\arctan(\eta)\right)\right] \cdot \exp\left[-\frac{\xi^2}{4s^2(1+\eta^2)}\right], \quad (13)$$

where $s_\tau(\tau) = s\sqrt{1+\eta^2}$ is the corresponding time-dependent width¹. After collecting the imaginary contributions from the prefactor and the complex exponent — the former is referred to as the Gouy phase, the phase dynamics are described by

$$\Phi_G(\xi, \tau) = \frac{\eta\xi^2}{4s^2(1+\eta^2)} - \frac{1}{2}\arctan(\eta). \quad (14)$$

For early times, when τ is sufficiently small, the Taylor expansion $\arctan(\eta) = \eta - \frac{1}{3}\eta^3 + \mathcal{O}(\eta^5)$ provides more interpretable insight into the specific polynomial phase behavior, yielding

$$\Phi_G(\xi, \tau) = \frac{\xi^2\tau}{2(4s^4 + \tau^2)} - \frac{\tau}{4s^2} + \frac{\tau^3}{48s^6}. \quad (15)$$

2.3. Airy–Airy Collision

To circumvent the limitation that only the density distribution of single quantum systems can be directly accessed in quantum mechanics, the interference of two wave packets is investigated. By carefully analyzing the

¹Noting that the previously defined width is in general a complex quantity, hence this second definition is real.

structure of the interference fringes, information about the underlying phase dynamics can be extracted. One simple interference scenario is the collision of two counterpropagating Ai-BECs in free space, since they naturally accelerate towards each other without requiring any initial momentum or external potential.

The superposition of two independent quantum mechanical objects, here chosen $\Psi_1 = \Psi_{Ai,1}$, $\Psi_2 = \Psi_{Ai,2}$ w.l.o.g., is described by

$$\Psi_{tot} = \Psi_{Ai,1} + \Psi_{Ai,2}. \quad (16)$$

Thus, the measurement of the probability density is

$$|\Psi_{tot}|^2 = |\Psi_{Ai,1}|^2 + |\Psi_{Ai,2}|^2 + 2|\Psi_{Ai,1}||\Psi_{Ai,2}| \cdot \cos(\Delta\Phi(\xi, \tau)), \quad (17)$$

with relative phase $\Delta\Phi(\xi, \tau) = \arg(\Psi_{Ai,1}) - \arg(\Psi_{Ai,2})$. For this particular experiment, the phase dynamics are

$$\begin{aligned} \Delta\Phi_{Ai-Ai}(\xi, t) = & -\frac{\tau_1^3}{12} + \frac{\tau_1 \xi_1}{2} + \frac{a_1^2 \tau_1}{2} \\ & + \frac{\tau_2^3}{12} - \frac{\tau_2 \xi_2}{2} - \frac{a_2^2 \tau_2}{2} \end{aligned} \quad (18)$$

with $\tau_i = \frac{t}{\tau_{0,i}}$, where $\tau_{0,i}$ ($i = 1, 2$) sets the individual Airy scale of each packet. Transforming the characteristic time scales according to $\tau_{0,i} = mx_{0,i}^2/\hbar$, the leading cubic coefficient reads

$$c_{3,Ai-Ai} = \frac{\hbar^3}{12m^3} \left(\frac{1}{x_{0,2}^6} - \frac{1}{x_{0,1}^6} \right). \quad (19)$$

2.4. Airy–Gaussian Collision

Another configuration that appears within experimental reach is the collision of an Airy and a Gaussian wave packet, again without requiring any initial momentum or external potential. The resulting phase difference is

$$\begin{aligned} \Delta\Phi_{Ai-G}(\xi, t) = & +\frac{\tau_{Ai}^3}{12} + \frac{\tau_G^3}{48s^6} - \frac{\tau_G}{4s^2} - \frac{\tau_{Ai}\xi_{Ai}}{2} \\ & - \frac{a^2\tau_{Ai}}{2} + \frac{\xi_G^2\tau_G}{2(4s^4 + \tau_G^2)} \end{aligned} \quad (20)$$

with $\tau_{Ai} = \frac{t}{\tau_{0,Ai}}$ and $\tau_G = \frac{t}{\tau_{0,G}}$. Accordingly, upon restoring physical units, the spatially uniform cubic coefficient is given by

$$c_{3,Ai-G} = \frac{\hbar^3}{m^3 x_0^6} \left(\frac{1}{12} + \frac{1}{48s^6} \right). \quad (21)$$

2.5. Heterodyne Phase Extraction

Extracting the phase could theoretically be performed directly via accessing the phase of the separately propagated wave packet amplitudes in the simulation, which are later added for the superposition. However, an experimentally feasible way to obtain the phase dynamics

is used here. Motivated by the interference cross term $\propto \Psi_2^* \Psi_1$ in the density of two overlapping condensates [5], the complex signal S_{HPE} is defined as a windowed overlap integral that characterizes the coherence between the two wave packets,

$$S_{HPE}(\tau) = \int w(\xi) \Psi_2^*(\xi, \tau) \Psi_1(\xi, \tau) e^{-ik_f(\xi - \xi_c(\tau))} d\xi, \quad (22)$$

where $w(\xi, \tau) = \exp\left(-\frac{1}{2} \frac{(\xi - \xi_c(\tau))^2}{\sigma_{ROI}^2}\right)$ denotes a Gaussian envelope as the region of interest (ROI) centered around the current peak of the overlap ξ_c with a width σ_{ROI} of order 10^{-2} to 10^{-1} in dimensionless units, and $k_f = k_{c,1} - k_{c,2}$ as the differential fringe carrier originating from a local plane-wave approximation discussed in the next subsection. This approach extends simple overlap measurements by incorporating a Gaussian spatial filter $w(\xi, \tau)$ and symmetrized fringe carrier compensation [36], enabling localized sensitive phase extraction.

Even though experimental execution prohibits the direct access of quantum mechanical amplitudes entering S_{HPE} on the level of the wave function, the cross term $\Psi_2^* \Psi_1$ could in principle be reconstructed in a heterodyne, phase-shifting interferometric scheme from two measurements at controlled relative phases [37]. The desired relative phase is finally obtained as

$$\phi_{rel}(\tau) = \text{unwrap}(\arg[S_{HPE}(\tau)]), \quad (23)$$

where $\arg(\cdot)$ denotes the complex argument and $\text{unwrap}(\cdot)$ implements numerical phase unwrapping to enforce temporal continuity.

2.6. Density-based Phase Extraction

A more practicable approach is the density-based phase extraction, because merely simple density profile measurements are required. Defining the superposition density

$$\rho(\xi, \tau) = |\Psi_1|^2 + |\Psi_2|^2 + 2 \Re[\Psi_2^* \Psi_1], \quad (24)$$

[5] and inserting the polar decomposition $\Psi_j(\xi, \tau) = |\Psi_j(\xi, \tau)| e^{i\Phi_j(\xi, \tau)}$, one obtains

$$\rho(\xi, \tau) = |\Psi_1|^2 + |\Psi_2|^2 + 2 A(\xi, \tau) \cos(\Delta\Phi(\xi, \tau)), \quad (25)$$

where $A(\xi, \tau) = |\Psi_1(\xi, \tau)| |\Psi_2(\xi, \tau)|$ denotes the local interference amplitude, which is assumed to vary slowly on the scale of the fringe spacing, and $\Delta\Phi(\xi, \tau) = \Phi_1(\xi, \tau) - \Phi_2(\xi, \tau)$ encodes the relative phase dynamics. To isolate the fringe contribution, a windowed fluctuation signal is defined as

$$\rho_{fluc}(\xi, \tau) \approx w(\xi) [\rho(\xi, \tau) - \rho_{mean}(\tau)], \quad (26)$$

with the local mean density $\rho_{mean}(\tau) = \frac{\int w(\xi) \rho(\xi, \tau) d\xi}{\int w(\xi) d\xi}$. In the region of interest, the phase is subsequently locally

approximated by a plane wave with a time-dependent offset,

$$\Delta\Phi(\xi, \tau) \approx k_f(\tau)[\xi - \xi_c(\tau)] + \phi(\tau), \quad (27)$$

which motivates the definition of the density-based complex signal [36]

$$S_{\text{DPE}}(\tau) = \int \rho_{\text{fluc}}(\xi, \tau) e^{-ik_f(\tau)[\xi - \xi_c(\tau)]} d\xi \quad (28)$$

including again the demodulation of the carrier frequencies in order to refine the pure, global phase. In addition, it is worth noting that the differential fringe carrier, consisting of $k_{c,1}$ and $k_{c,2}$, is obtained from calibration measurements performed on the single wave packets, which allows the extraction of the peak position in momentum space separately. The peak overlap density position $\xi_c(\tau)$ is visually obvious from the straight, quasi-stationary interference fringe, for example of the two main lobes, and hence this stable and well-defined position can be reliably approximated by the peak position of the total superposition density, owing to the sharp shape of the Airy main lobes – for the Airy-Gaussian collision the procedure is analogous. Eventually, the relative phase is obtained from $S_{\text{DPE}}(\tau)$ via the same argument and phase-unwrapping method as in the previous subsection.

3. SIMULATION MEASUREMENTS

In the following passage, the Ai-Ai and the Ai-G collision phase dynamics are studied – in particular by two types of phase extraction, which both are experimentally feasible – here demonstrated in simulations.

3.1. Cubic Airy–Airy Phase

After the phase extraction had been carried out – here by selecting a narrow Gaussian ROI with a width of $\sigma_{\text{ROI}} = 0.01$ for the heterodyne phase extraction (HPE) and signal demodulation by removing the linear carrier frequency, the argument of the resulting complex signal, which is rendered continuous by phase unwrapping, corresponds to the pure phase. For quantitative analysis, only connected regions – such as the first interference fringe of the main lobes in Fig. 1, ranging from approximately 0.4 ms to 0.6 ms² – are considered for modeling the phase dynamics. The phase data are analyzed using a centered generalized least-squares fit of a third-order polynomial. This procedure yields the polynomial coefficients, their covariance matrix, and hence their standard errors.

In Fig. 2, the deviations of the fitted cubic coefficient c_3 from its theoretical value $c_{3,\text{theo}}$, based on the heterodyne simulation phase extraction, are shown. The x-

²The initial separation of the two Airy profiles is chosen sufficiently small to increase the temporal overlap of the main-lobe interference fringe. At early times the lobes have accelerated only weakly, so their relative velocity is small, which tends to prolong the overlap.

and y-axes characterize the choice of the fitting interval, defining each point on the map by one unique pair of the starting and end time of the fitting region. The general, global structure is a rather steep valley of minima extending from the upper left corner towards the lower right corner. The area below this valley exhibits rapidly increasing positive deviations, while the opposite upper region – above the valley – shows increasingly negative deviations, noting that this metaphor focuses on the absolute deviations, disregarding their sign. The contour lines of constant relative deviation of 5 % and of 10 % are laid relatively close to the line of optimal fit values. The top 20 fit values are approximately equally distributed in the upper part, favoring rather larger regions, but this effect might also very likely be caused by the finite numerical resolution. The best fitting point is located at $t_{\text{start}} \approx 0.38$ ms, $t_{\text{end}} \approx 0.50$ ms. Apart from numerical instabilities for very small fitting windows, corresponding to weakly determined fitting conditions along the boundary of the lower, right triangle, the overall landscape is free from random fluctuations or disturbances, providing high confidence in the trend analysis.

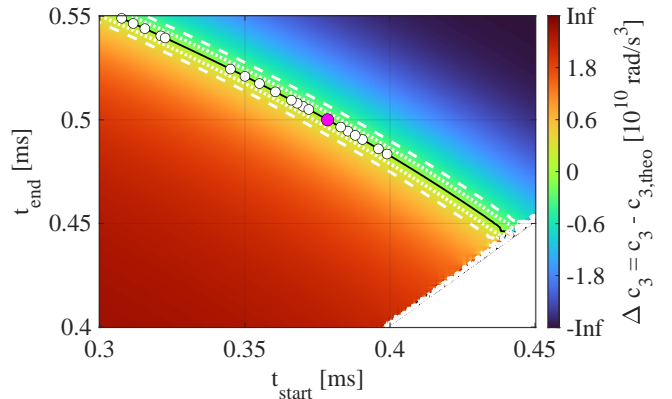


Figure 2. Deviation of $\Delta c_3 = c_3 - c_{3,\text{theo}}$ across $[t_{\text{start}}, t_{\text{end}}]$ for the Ai-Ai collision scenario, representing the robustness of the phase extraction visualizing the sensitivity of the cubic coefficient c_3 on the fitted region based on the heterodyne phase extraction. Two white, drawn contour lines mark the relative error of 5% (dotted) and 10% (dashed). The highlighted data points show the best combinations among these discrete pairs due to the finite resolution. The pink dot represents the closest value to $c_{3,\text{theo}} = -3.472800 \times 10^{10} \text{ rad/s}^3$. The colour indicates the signed, nonlinearly compressed deviation $\Delta c_3 = c_3 - c_{3,\text{theo}}$, using $T = \text{sgn}[\tanh(k \Delta c_3/2s)] |\tanh(k \Delta c_3/2s)|^\gamma$ with $k = 2.5$, $\gamma = 0.7$, and s given by the 90th percentile of $|\Delta c_3|$, which provides a symmetric, bounded, contrast-enhanced colour scale for Δc_3 and compresses outliers.

The best-fitting choice in Fig. 3 exhibits a slight cubic curvature. Compared to Fig. 1, the preferred fit window does not cover the full temporal range of the interference fringe of the two main lobes. This can be attributed to the growing influence of the second-largest interference fringe, extending from 0.53 ms to 0.63 ms as

an area of appreciable magnitude with a certain spatial width, hence affecting the measured ROI.

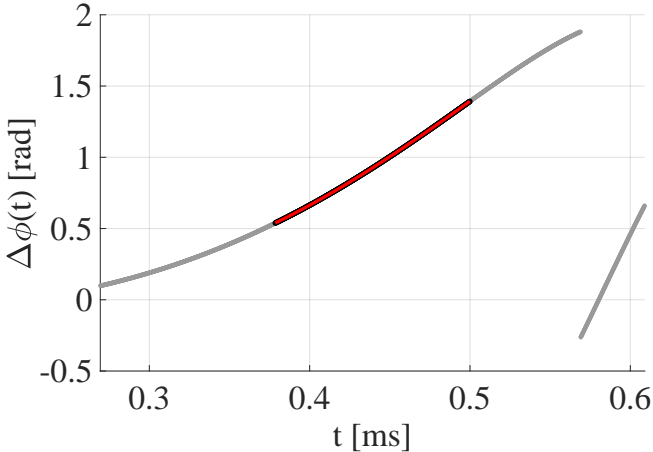


Figure 3. Relative phase of Airy main lobe interference fringe from the demodulated signal of the HPE – continuing the Ai-Ai collision scenario. The best cubic fit window choice, corresponding to the pink dot of Fig. 2, is drawn in red relying on the highlighted data in black.

Within the considered time window $t \in [0, 1]$ ms regarding the best fit coefficient in Table 1, the contributions $c_i t^i$ of all polynomial orders are of comparable magnitude, except for the rather small cubic contribution, so the phase dynamics cannot be described as purely cubic. Nevertheless, the fit requires a non-zero cubic term c_3 with high statistical significance. In general, the coefficients are well-determined considering the associated uncertainties which are reasonably small.

Since the heatmap here is initially calibrated for the case $g = 0$, the cubic coefficient matches the theoretical value for the accordingly chosen fit intervals along the valley, and thus the main focus should not lie on the matching of the mean value of the top simulation measurements of the valley but rather on the insights revealed by the structure of the robustness heatmap. In addition, only the comparison of the cubic coefficient to its theoretical prediction is advisable, since the lower order coefficients are highly influenced by the demodulation that attempts to subtract the local linear term. Consequently, the lower order coefficients are treated as nuisance parameters, and the focus lies on the cubic term.

Table 1. Best-fit coefficients for the Ai-Ai phase dynamics from the HPE, corresponding to the pink dot of Fig. 2. The last column shows the order of magnitude of the phase contributions $|c_i t^i|$ at $t = 0.10$ ms. Numbers in parentheses denote 1σ uncertainties in the last digits (e.g. $-3.47(3) \times 10^{10} \equiv (-3.47 \pm 0.03) \times 10^{10}$).

Coefficient	Value \pm Standard Error	Unit	$ c_i t^i $ [rad]
c_3	$-3.47(3) \times 10^{10}$	rad/s^3	10^{-2}
c_2	$5.67(4) \times 10^7$	rad/s^2	10^{-1}
c_1	$-2.252(18) \times 10^4$	rad/s	10^0
c_0	$2.826(26)$	rad	10^0

When performing a third-order polynomial fit, the cubic coefficient is particularly sensitive to the selected input data, since the fitted range here lies within a region where the cubic term exhibits an inverted gradient compared to the dominant global trend. This sensitivity becomes especially pronounced when only a few data points are available due to the finite temporal extent of the interference fringe. In this case, a symmetric selection of data points around the inflection point is crucial, avoiding an overweighting of one curved tail of the fitted region. Any asymmetry disturbs the fitting process relying on the essential underlying determination of the curvature, which is therefore directly reflected in c_3 . Thus, the prevention of this effective bias in the extracted cubic coefficient is important.

The hypersensitivity of the fitted cubic c_3 is illustrated in Fig. 2, where high accuracy with respect to the theoretical value $c_{3,\text{theo}}$ is achieved only for specific symmetrical pairs of start and end times. The necessity of such symmetrized data selection is evident from the negative slope of the minima in the deviation from the theoretical $c_{3,\text{theo}}$. Accordingly, for a fixed t_{start} , a larger t_{end} adds more data points to the right tail, hence increasing the leverage of late-time points, biasing the estimate toward smaller c_3 for a globally more negative trend of the phase, and vice versa.

For comparison with HPE, the experimentally simpler density-based phase extraction (DPE) is applied in the following, where σ_{ROI} is set to 0.34 for an optimal extraction. The heat map in Fig. 4 lets one recognize a similar valley structure despite an enlarged region of fit instability of the fit in the lower right section. This divergence region for small fit interval choices appears to be method-inherent, since it does barely vanish for optimized parameter choices shown in Fig. 4. Surprisingly, the upper area does not diverge to high negative deviations from $c_{3,\text{theo}}$, but is restricted by the valley structure returning in form a u-shaped curve. This behavior appears to be linked to the choice of σ_{ROI} and could be explored further by a parameter scan. Moreover, the contour lines are less tightly packed around the minima, like the overall contour lines for HPE, for larger fitting windows, possibly explained by the fact that more data tend to cause a more stable and robust fit with respect to the fit window selection. Overall, the HPE distinguishes itself from the DPE by its higher accuracy evident from the differences of the two heat scales. The best-fit choice has a very similar location with $t_{\text{start}} \approx 0.38$ ms, $t_{\text{end}} \approx 0.45$ ms.

When using the two phase-extraction methods, the best parameter choices differ: The HPE achieves optimal robust and precise c_3 estimates for very small σ_{ROI} , which is reasonable since it directly accesses the reconstructed amplitudes and works best with only few spatial data points that carry the phase information. This corresponds to a narrow envelope, avoiding large σ_{ROI}

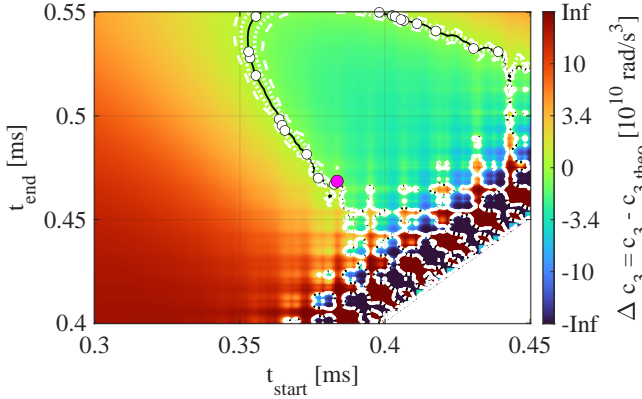


Figure 4. Deviation of $\Delta c_3 = c_3 - c_{3,\text{theo}}$ across $[t_{\text{start}}, t_{\text{end}}]$ for the Ai–Ai collision scenario, based on the DPE. As in Fig. 2, the axes parameterize the fit window, the white contour lines indicate relative errors of 5% (dotted) and 10% (dashed), and the highlighted points mark the best discrete window combinations, with the pink dot denoting the closest value to $c_{3,\text{theo}}$. The region of small fit interval choices oscillates and diverges due to fit instability. The colour scale uses the same signed, nonlinearly compressed mapping of Δc_3 as in Fig. 2.

that would include ‘noisier’ regions further away from the peak of the interference fringe, where the local plane-wave approximation becomes increasingly inaccurate. In contrast, the DPE works at its optimum for larger σ_{ROI} , because the spatial averaging of ρ_{mean} in $S_{\text{DPE}}(\tau)$ requires a sufficiently large area to efficiently cancel out local fluctuations and small-scale variations, and to average over experimental noise, in order to provide the background which is subtracted from the pure density to obtain the evolution in Eq. 26. However, this larger Gaussian window also introduces the influence of neighbouring interference fringes as a systematic bias entering ρ_{mean} and decreasing the quality in terms of signal-to-noise ratio of this quantity, which affects the robustness-map structure and increases the error bars of the fit coefficients, as seen in Table 2. Therefore, the parameters are adjusted separately for each method to minimize variance and maximize stability.

Furthermore, the combined effect of the bias from adjacent fringes entering as a systematic error, and the local plane-wave approximation used to define the carrier leads to DPE uncertainties that are systematically larger than (or at best comparable to) the HPE benchmark. In particular, the minimal DPE uncertainty observed in the robustness map does not fall below the corresponding HPE value.

In addition, another major difference is that the best-fit for DPE in Fig. 5 is not centered around the inflection point, assuming the underlying phase dynamics from HPE in Fig. 3 provide a clear, extracted signal as a good approximation of the true phase dynamics governing also this second case. Particularly since the fitted data are not very similar, which may be due to the fun-

damentally different phase extraction methods, a deeper examination would be necessary to infer conclusions with high confidence and to differentiate between various contributions. Fig. 5, in combination with the evolution in Fig. 1, suggests that spatially well-separated data with a clear distance to other interference patterns are favored in order to obtain the most pure signal and therefore constraining possible fit windows, since the best fit time interval does not cover the whole interference fringe – otherwise, the curvature of the phase dynamics is distorted.

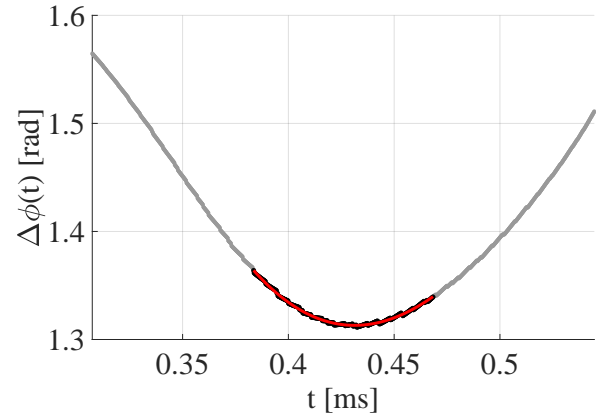


Figure 5. Relative phase of the Airy main lobe interference fringe from the demodulated DPE signal for the Ai–Ai collision scenario. The best cubic fit window is shown in red and is based on the highlighted data points in black. This interval falls within the cubic regime, where the local slope reverses relative to the global trend.

The DPE-fit coefficients show significantly larger uncertainties, while the cubic term still agrees with the theoretical value. In particular, the standard errors are increased by about one order of magnitude, which originates in the fundamentally less precise extraction technique involving averaging and approximations. In general, this density-based method is still an elegant approach to access information about the phase dynamics with reasonable output measurements.

Table 2. Fit coefficients of Ai–Ai phase dynamics (DPE) at the best-fit window, corresponding to the pink dot in Fig. 4. The last column shows the order of magnitude of the phase contributions $|c_i t^i|$ at $t = 0.10$ ms.

Coefficient	Value \pm Standard Error	Unit	$ c_i t^i $ [rad]
c_3	$-3.5(4) \times 10^{10}$	rad/s^3	10^{-2}
c_2	$6.6(5) \times 10^7$	rad/s^2	10^{-1}
c_1	$-3.72(21) \times 10^4$	rad/s	10^0
c_0	$7.94(29)$	rad	10^0

3.2. Cubic Airy–Gaussian Phase

In Fig. 6 a sharply peaked Gaussian BEC is superimposed with the main lobe of an Ai–BEC. For analyzing the collision, σ_{ROI} is set to 0.20 for HPE and 0.21 for DPE, because the spatial extension of the Gaussian wave

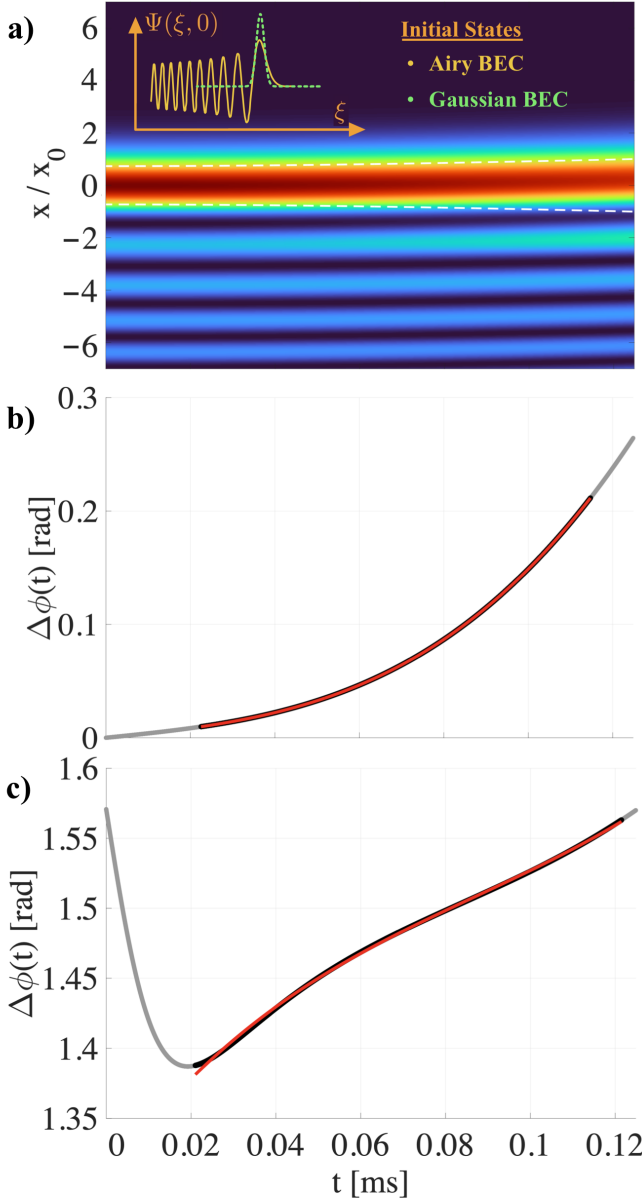


Figure 6. Time evolution of probability density profile $|\Psi(x, t)|^2$ in free space, shown in a): Interference of an Ai-BEC and a Gaussian wave packet creating an initial overlap with the main lobe of the Airy profile. The white contour line marks the evolving one-sigma-width of the dispersing Gaussian packet.

Relative phase of the overlap region from the demodulated b) HPE and c) DPE signal for the Ai-G collision. The best cubic fit window is shown in red and is based on the black data points.

packet has to be covered well-enough in the measurement. Both robustness maps in Fig. 7 exhibit a noiseless valley structure similar to the HPE-based Ai-Ai scenario, which is the closest simulated description to the theory of the Ai-Ai case here available. Moreover, there is a sharp bend upwards in the valley structure in the vertical direction for both methods. For HPE fitting windows with $t_{\text{start}} \approx 0.017$ ms, there appear to be several best choices for t_{end} starting with the lowest at 0.125 ms till

the boundary of the heatmap. A similar behavior with slightly different values is observed for the DPE case. In combination with the slightly decreased slope of the minima valleys for HPE and an apparently reduced slope for DPE, this might suggest avoiding early measurement data but allowing a rather generous choice of the final boundary. Especially, the robustness is remarkable since for both extraction methods large regions of the heatmaps show deviations in the order of 10^8 - equating approximately three orders smaller than the theoretical value $c_{3,\text{theo}} = 1.161642 \times 10^{11}$ rad/s³. The best fit simulation measurement is $(1.16164 \pm 0.00009) \times 10^{11}$ rad/s³ for HPE and $(1.16 \pm 0.19) \times 10^{11}$ rad/s³ for DPE with the smallest deviations to the theoretical value. The other top 19 values are seemingly equally distributed for HPE and DPE except for short fitting intervals, requiring again a minimum level of data for an accurate fit, and early time inclusion. For HPE, the contour lines are not even drawn, and for DPE they enclose a noticeably area around the minima valley.

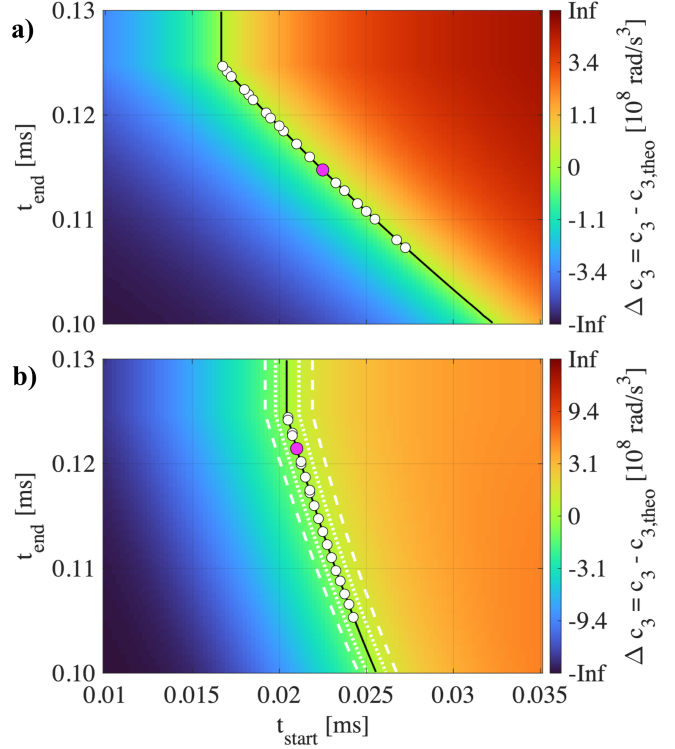


Figure 7. Deviation of $\Delta c_3 = c_3 - c_{3,\text{theo}}$ across $[t_{\text{start}}, t_{\text{end}}]$ for the Ai-G collision, based on the a) HPE and b) DPE. As in Fig. 2, the axes parameterize the fit window, the white contour lines indicate relative errors of 5% (dotted) and 10% (dashed), and the highlighted points mark the best discrete window combinations, with the pink dot denoting the closest value to $c_{3,\text{theo}}$. The colour scale uses the same signed, non-linearly compressed mapping of Δc_3 as in Fig. 2.

Regarding the relative phase data and their best fit windows in Fig. 6 b) and c), the two extraction methods share the same general ascending, nonlinear trend. However, the DPE phase data start with an irregular peak

for early times. Both best fit choices use a time interval starting approximately at $t_{\text{start}} = 0.02$ ms, and hence DPE excludes this artefact.

The cubic coefficients of Table 3 and 4 agree with $c_{3,\text{theo}} = 1.161642 \times 10^{11}$ rad/s³. The HPE suggests a strong dominance of the cubic term over its nuisance parameters, due to the enhanced cubic contributions in comparison to the Ai-Ai case. The reason seems to originate in the asymmetry of the collision – not cancelling out the corresponding cubic phase term in Eq. 21, unlike Eq. 19 motivates for Ai-Ai. Therefore, an excessive, dominant role of the Kennard phase can be achieved – here by approximately one order of magnitude over the linear term and two orders over the quadratic term, enabling the HPE observer to clearly differentiate between the polynomial contributions and accessing the precious Kennard phase coefficient. For DPE in Table 4, the contributions are not as divergent as for HPE, potentially because of the concave artefact bulge in the phase data at $t = 0.05$ ms, but still in the same order – neglecting the irrelevant offset, such that the cubic contribution is well expressed to be extracted.

Summarizing the emergent picture, it can be concluded that rather small differences for the Ai-G collision across the different techniques, HPE and DPE, can be noticed, in contrast to the sharp distinction to the Ai-Ai scenario based on the asymmetry in the phase dynamics of Ai-G.

Table 3. Fit coefficients of Ai-G phase dynamics (HPE) at the best-fit window, corresponding to the pink dot in Fig. 7 a). The last column shows the order of magnitude of the phase contributions $|c_i t^i|$ at $t = 0.10$ ms.

Coefficient	Value \pm Standard Error	Unit	$ c_i t^i $ [rad]
c_3	$1.16164(9) \times 10^{11}$	rad/s ³	10^{-1}
c_2	$-8.173(18) \times 10^5$	rad/s ²	10^{-3}
c_1	$4.1152(12) \times 10^2$	rad/s	10^{-2}
c_0	$-3.938(22) \times 10^{-4}$	rad	10^{-4}

Table 4. Fit coefficients of Ai-G phase dynamics (DPE) at the best-fit window, corresponding to the pink dot in Fig. 7 b). The last column shows the order of magnitude of the phase contributions $|c_i t^i|$ at $t = 0.10$ ms.

Coefficient	Value \pm Standard Error	Unit	$ c_i t^i $ [rad]
c_3	$1.162(19) \times 10^{11}$	rad/s ³	10^{-1}
c_2	$-3.26(4) \times 10^7$	rad/s ²	10^{-1}
c_1	$4.382(22) \times 10^3$	rad/s	10^{-1}
c_0	$1.3034(4)$	rad	10^0

In contrast to the Ai-Ai collision, the generally shown time evolution of interest is much smaller due to the rapid dispersion of the peaked Gaussian packet, but the length of the fitted time interval is in a similar order of $t_{\text{fit-interval}} \approx 0.1$ ms for both types of collisions.

In addition, the Ai-G phase extraction distinguishes from the Ai-Ai algorithm by eventually subtracting a ge-

ometric correction $\phi_{\text{geom}}(\tau) = k_f(\tau) \xi_c(\tau)$ of the refined phase to obtain the corrected phase

$$\phi_{\text{corr}}(\tau) = \phi_{\text{rel}}(\tau) - \phi_{\text{geom}}(\tau). \quad (29)$$

This term originates in the centered demodulation, whose purpose is to make the extraction robust to small errors in the determination of k_f , in Eq. 22 and 28. An uncentered demodulation could cause phase ramps $e^{-i(k_f,\text{true} + \Delta k_f)\xi}$ across the Gaussian window, which would enter as a systematic bias in the measured amplitude and phase. The centered method provides – in case of a slightly misdetermined k_f – a symmetrical ramp which mostly cancels out. For the Ai-Ai case, the evolution – apart from the small difference of the Airy length scales – is highly symmetric, and therefore k_f is a small quantity. In addition, the interference fringe is quasi-stationary in Fig. 1 resulting in an almost constant $\xi_c(\tau) = \xi_{c,\text{fringe}}$, and thus the spatially and timely independent phase factor becomes a physically irrelevant offset of the phase, which does not require any major correction. Hence, the phase of the asymmetric Ai-G scenario needs to be corrected. Furthermore, for consistency with the cubic phase model, the higher-than-third-order remainder of the Gaussian Gouy term $-\frac{1}{2} \left[\arctan(\eta) - \left(\eta - \frac{\eta^3}{3} \right) \right]$ is subtracted from $\phi_{\text{corr}}(\tau)$ prior to fitting. Unlike the Ai-Ai case, the Ai-G phase does not exhibit a local slope opposite to the overall trend within the fit window, which also makes the fitting procedure significantly more robust as seen in the heatmaps.

For Ai-Ai, a slight asymmetry in the Airy length scale scales between the two Airy packets is introduced to avoid an exact cancellation of the relative cubic phase. Nevertheless, the cubic phase contribution in the highly symmetric Ai-Ai collision remains small compared with lower-order terms, such that finite-window limitations and extraction systematics make isolating the cubic dynamics comparatively fragile. This highlights a trade-off in the collision design: a more symmetric Ai-Ai configuration improves cancellation of nuisance contributions and makes geometric phase corrections largely irrelevant, but it also suppresses the net cubic signal. In contrast, the intentionally asymmetric Ai-G collision yields a dominant cubic phase contribution, which substantially improves robustness and parameter separability in the polynomial fit.

The major difference of both constructed collisions is their robustness, the improved, less window-sensitive accuracy, and their precision of the cubic coefficient primarily owing to its dominant contribution. The overall significantly higher robustness of the Ai-G collision – in particular two orders of magnitude less sensitive to the fit interval selection, and the congruence of both Ai-G robustness maps of the HPE and the DPE, in comparison with the obvious differences for Ai-Ai, recommend the Ai-G case with DPE as the preferred simplest sce-

nario to study, again reminding of the assumption that the HPE method is the technique providing the closest measurement describing the corresponding analytically derived theoretical model. A further advantage is the higher precision for Ai-G. Despite of a more than twice larger $c_{3,\text{theo}}$ of Ai-G compared to Ai-Ai, the relative as well as the absolute standard deviations are significantly smaller for Ai-G-HPE and Ai-G-DPE, which can be explained by the not only window-robust, but enhanced stable fit due to the dominant cubic phase, corresponding to the asymmetry of the collision effecting the phase dynamics. For instance, the experimentally preferred DPE yields standard errors of $\Delta c_{3,\text{Ai-G}} = 1.9 \times 10^9 \text{ rad/s}^3$ and $\Delta c_{3,\text{Ai-Ai}} = 4 \times 10^9 \text{ rad/s}^3 \approx 2 \cdot \Delta c_{3,\text{Ai-G}}$, equating to the relative errors of 1.64 % for Ai-G and 11.43 % for Ai-Ai.

3.3. Uncertainty Estimation

In order to test the nonlinearity influence experimentally, choosing one best fit window is naive even though an accurate calibration of $g = 0$ might provide the valley structure of the robustness heatmap. In general, suboptimal conditions should be assumed to maintain a conservative attitude, and therefore the experimental circumstances might create noisy heatmaps with enhanced small-scale fluctuations – generally meaning a worse signal-to-noise ratio of the initial underlying data. Thus, not a single best fit point, which would correspond to a single fit window, should be selected since the cubic coefficient is hypersensitive even to small time interval changes, but rather an average over several values – for instance by simply fixing the value t_{start} and varying the upper boundary t_{end} , to avoid selecting a noise-induced minimum instead of the perfect minimum in an ideal valley cross-section. The sampling range should, as far as possible, be centered around the valley structure and should ideally contain only a limited number of values. The choice of this range should be based on a trade-off between deliberately including points with small deviations, which may cancel due to positive and negative deviations around the minimum, and ensuring a sufficient number of data points to cope with noise.

However, naively simple averaging would intrinsically yield a mean with an enormously underestimated uncertainty since these coefficients rely on data windows which are highly correlated, and hence reasonably concluding that c_3 is subjected to the same correlations. At this point, it's worth noting that – as all the heatmaps illustrate well – the hypersensitivity of the cubic coefficient does not compensate the correlation effects, apart from the necessary perfect match of their contrary magnitude of both effects, because it refers to the accuracy and not its precision, the uncertainty. In case of a single point extraction, a noise-induced, slightly displaced position in the heatmap not providing the perfect fit window with the true c_3 value can heavily distort succeeding non-

linearity measurements because of the hypersensitivity. Even neighbouring points in the heatmap can have noticeably other values, again reminding of the compressed representation of the deviations by the colours, which enable the overview of rapid changes.

In order to obtain a realistic uncertainty estimate of the algorithm-based systematics, the heteroskedasticity and autocorrelation consistent (HAC) Newey-West estimator is used [38]. It considers correlation by introducing corrections to the covariance matrix. Each fit of the relative phase data over a certain time interval yields an estimate $c_{3,i}$ with an associated fit uncertainty SE_i . Then, the unweighted mean $\mu = \frac{1}{m} \sum_{i=1}^m c_{3,i}$ is constructed to determine the corresponding residuals $r_i = c_{3,i} - \mu$. Thus, the autocovariances up to lag L can be defined as

$$\hat{\gamma}_\ell = \frac{1}{m - \ell} \sum_{i=1}^{m-\ell} r_i r_{i+\ell}, \quad \ell = 0, 1, \dots, L, \quad (30)$$

to account for serial correlation between neighbouring windows, and subsequently applying the Bartlett weights

$$w_\ell = 1 - \frac{\ell}{L+1}, \quad \tilde{\gamma}_\ell = w_\ell \hat{\gamma}_\ell. \quad (31)$$

From $\tilde{\gamma}_\ell$, a Toeplitz process covariance matrix is assembled,

$$(\Sigma_{\text{proc}})_{ij} = \begin{cases} \tilde{\gamma}_{|i-j|} & |i - j| \leq L, \\ 0 & \text{otherwise,} \end{cases} \quad (32)$$

The heterogeneous fit uncertainties enter as an additional diagonal term,

$$\Sigma = \Sigma_{\text{proc}} + \text{diag}(\text{SE}_1^2, \dots, \text{SE}_m^2), \quad (33)$$

so that Σ represents a realistic covariance matrix of the vector $\mathbf{c} = (c_{3,1}, \dots, c_{3,m})^\top$, combining process correlations and window-dependent measurement noise. Eventually, the standard error is given by

$$\text{SE}(\hat{\mu}) = (\mathbf{1}^\top \Sigma^{-1} \mathbf{1})^{-1/2}, \quad (34)$$

with the mean estimate $\hat{\mu} = \frac{\mathbf{1}^\top \Sigma^{-1} \mathbf{c}}{\mathbf{1}^\top \Sigma^{-1} \mathbf{1}}$ and $\mathbf{1} = (1, \dots, 1)^\top$. This approach yields a conservative and data-driven uncertainty estimate, which considers both serial correlation and heterogeneous fit uncertainties, and which should be regarded only as a lower bound of the actual experimental uncertainty – focusing here only on the algorithm-systematics.

Generally, since the majority of underlying data are shared with the adjacent window, substantial serial correlation is expected, motivating the use of relatively large lags L – up to $L = m - 1$. However, for L approaching m , the number of terms contributing to the each autocovariance estimate in Eq. 30 decreases, making high-lag estimates increasingly noisy. Thus, finite window

sizes can limit accounting properly for strong correlation. The Bartlett weights downweight these high-lag contributions, which helps to regularize the HAC covariance estimate and to keep it well behaved – in particular, the Newey–West construction yields a positive semidefinite estimate [38]. In practice, long-range correlations can also lead to partial cancellation in the residual products summation because of opposing signs, causing negative contributions, so that increasing L does not necessarily increase the estimated uncertainty, here due to the heatmap valley structure. Because c_3 is highly sensitive to the selected interval, the mapping from window overlap to correlations in c_3 need not be straightforward. The HAC Newey–West estimate should therefore be interpreted empirically as a conservative, data-driven standard-error correction for window-induced correlation, rather than a complete account of all algorithmic, protocol-induced uncertainties.

For a careful analysis, the L , that maximizes the uncertainty is chosen, which is exemplified with $\hat{c}_{3,\text{HAC}} = (1.160 \pm 0.025) \times 10^{11} \text{ rad/s}^3$ for $L = 14$, $m = 28$ in Table 5. Hence, the Newey–West-corrected standard error is increased by 31.58%. The theoretical value $c_{3,\text{theo}}$ lies within the corresponding one-sigma interval and thus agrees with this Newey–West estimate.

Table 5. Heteroskedasticity and autocorrelation consistent uncertainty estimate for a fixed start time $t_{\text{start}} = 0.015 \text{ ms}$ with $m = 28$ windows, for the Ai-G collision with DPE.

L	$\hat{c}_{3,\text{HAC}} [10^{11} \text{ rad/s}^3]$	SE [10^9 rad/s^3]
3	1.16113	1.768
6	1.16081	2.146
8	1.16066	2.302
11	1.16053	2.442
14	1.16046	2.494
17	1.16039	2.468
20	1.16034	2.387
22	1.16033	2.307
25	1.16032	2.140

3.4. Nonlinearity Influence on Cubic Dynamic

Eventually, the influence of the scaling factor g of the nonlinearity on the cubic coefficient c_3 can be studied. In particular, $c_3(g)$ is extracted from the Ai-G collision using the DPE, and uncertainties are estimated via the HAC Newey–West procedure to obtain a conservative, systematics-informed error level.

Special attention is paid to experimentally motivated parameters: the rubidium-87 mass $m = 1.44 \times 10^{-25} \text{ kg}$ and the corresponding force of the eigenpotential for the initial Airy profile, $F = m a_{\text{grav}}$ with $a_{\text{grav}} = 9.81 \text{ m/s}^2$ used in the simulation.

The central data point in Fig. 8 corresponds to the calibration at $g = 0$. For $g < 0$, the wave packets exhibit attractive (focusing), bright-soliton-like behavior, whereas for $g > 0$ the interaction is repulsive (defocusing), leading to dark-soliton-like density notches.

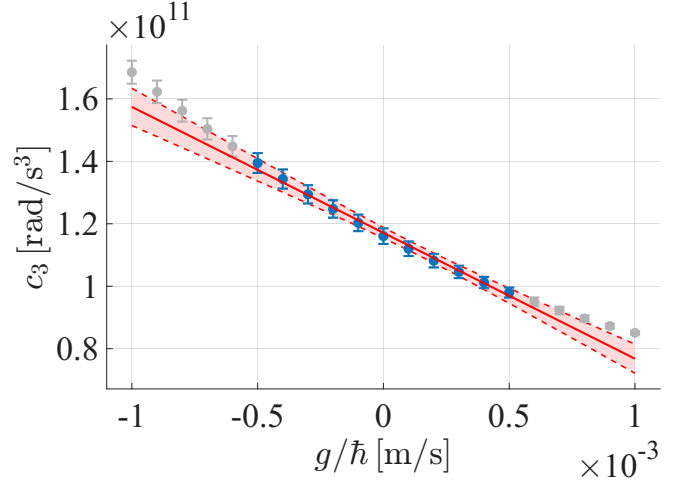


Figure 8. Cubic coefficient $c_3(g)$ as a function of the nonlinearity parameter g/\hbar , extracted from the Ai-G scenario using DPE with HAC Newey–West uncertainty and mean estimation. The blue-highlighted subset indicates the perturbative range used for the linear approximation. The red confidence band is bounded by the dashed red lines.

In the weakly nonlinear regime, the dependence of c_3 on the control parameter g is approximated by the leading term of a local perturbative expansion, $c_3(g) = c_3(0) + \alpha(g/\hbar) + \mathcal{O}(g^2)$, and the analysis is therefore restricted to a narrow window around $g = 0$. In particular, for $g/\hbar \in [-0.5 \times 10^{-3}, 0.5 \times 10^{-3}] \text{ m/s}$ the cubic coefficient can be modeled linearly in g to good approximation.³ Within the shown range, the estimated uncertainty of c_3 decreases for larger g .

A weighted least-squares fit of the linear model $c_3(g) = \alpha g/\hbar + \beta$ in the window $|g/\hbar| \leq 0.5 \times 10^{-3} \text{ m/s}$ with the weights $w_i = 1/\sigma_i^2$ yields $\alpha = (-4.033 \pm 0.012) \times 10^{13} \text{ rad m}^{-1} \text{ s}^{-2}$ and $\beta = (1.171 \pm 0.008) \times 10^{11} \text{ rad/s}^3$ with standard errors under the simplifying assumption of independent point-to-point errors.⁴

³For an order-of-magnitude context, in a quasi-one-dimensional BEC one has, to good approximation, $g_{1D}/\hbar \simeq 2\omega_{\perp}a_s$ in m/s, assuming $a_s \ll a_{\perp}$. For rubidium-87 with $a_s \approx 5.3 \text{ nm}$ and $\omega_{\perp}/2\pi \approx 5 \text{ kHz}$ this gives $g/\hbar \sim 10^{-4} \text{ m/s}$, and for $\omega_{\perp}/2\pi \approx 30 \text{ kHz}$ one obtains $g/\hbar \sim 10^{-3} \text{ m/s}$, so that the perturbative range considered here is plausibly experimentally accessible [39–41].

⁴The pointwise uncertainties σ_i are obtained from a Newey–West (HAC) estimate applied to the correlated time series underlying each averaged data point $c_3(g_i)$. The uncertainties are analytic, model-based standard errors due to the generalized least square fit. They are inferred from the residual scatter. No per-point phase uncertainties enter because phase noise is not explicitly modeled. In addition, the standard errors might ignore possible correlations among adjacent data points, so the fit is used as a phenomenological first-order approximation in the perturbative regime. The reduced chi-square obtained from the weighted fit is $\chi_{\text{red}}^2 = 0.195$. Values below unity can indicate that the quoted σ_i are conservative and/or that residual correlations between estimated points are not fully captured by a diagonal weighting. Therefore, χ_{red}^2 is primarily used as a qualitative consistency check and the assessment relies on the residual structure and fit-window stability to evaluate the adequacy of the linear approximation.

Within the chosen window, the residuals remain well below the quoted uncertainties – all points are within $\lesssim 1\sigma$, supporting the use of the linear approximation as a controlled first-order description of the response. At the same time, the residuals exhibit a weak, even-in- g curvature consistent with subleading $\mathcal{O}(g^2)$ corrections. Thus, the fitted slope α is interpreted as the leading perturbative response coefficient in the small- $|g|$ regime, rather than as evidence for a globally linear dependence.

Beyond $|g/\hbar| > 0.5 \times 10^{-3}$ m/s, the data clearly exhibit nonlinear behavior such that the linear approximation no longer holds. Accordingly, for larger $|g/\hbar|$ the linear model is underparametrized and higher-order corrections become necessary.

For the Ai-Ai case at stronger nonlinearity, the fringe pattern becomes dominated by mean-field effects: in particular, the phase extraction relying on the initial calibration requires an approximately constant fringe geometry, whose spatially fine interference structure however becomes progressively disturbed resulting in less accurate phase extraction until ultimately breaking down.⁵ In contrast, the initial overlap of the Airy main lobe and the Gaussian packet in the Ai-G configuration – shown here – remains substantially more robust. This motivates the Ai-G setup as a practical nonlinearity benchmark for probing the regime even beyond the perturbative limit.

3.5. Airy-Scale Parameter Sweep

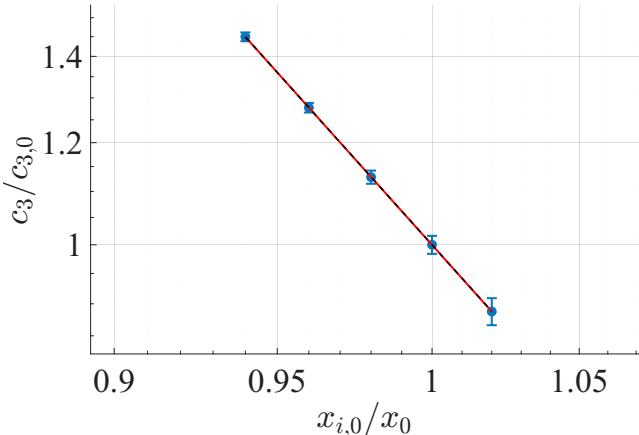


Figure 9. Log-normalized cubic coefficient $\log(c_3/c_{3,0})$ for the Ai-G scenario (HPE), shown as a function of the Airy scale $x_{i,0}$.

As an independent validation of the c_3 predictions obtained from the robustness heatmaps, the slope of $\log(c_3/c_{3,0})$ in Fig. 9 is found to be -6.005 ± 0.004 , confirming the predicted scaling $c_3 \propto x_0^{-6}$ in Eq. 21.

4. CONCLUSION

The interference of Airy-shaped Bose-Einstein condensate wave packets with each other (Ai-Ai) or with a Gaussian profile (Ai-G) in free space allows extracting information about the phase dynamics by analyzing the main interference fringe. Two experimentally feasible methods based on heterodyne or on pure density measurements can be used to investigate the peculiar, globally cubic time-dependence of the phase – also known as the Kennard phase. Therefore, the influence of the Gross-Pitaevskii-nonlinearity can be studied by adding a small perturbation in the conventional linear Schrödinger equation as an approximation of the Gross-Pitaevskii equation, which is implemented in the simulation via a split step method. Within $|g/\hbar| \leq 0.5 \times 10^{-3}$ m/s, the cubic coefficient of the phase dynamics exhibits a linear dependence in g/\hbar .

The asymmetric Ai-G configuration enhances the cubic contribution, is significantly more robust to the fit-window choice than the more fragile, near-symmetric Ai-Ai case, and is enabling accessing the Kennard phase with high precision. Within each collision, the heterodyne phase extraction is at least one order of magnitude more precise than the density-based phase extraction, which still yields reasonably small uncertainties and is experimentally easier to access. Overall, Ai-G is about one order of magnitude more precise than Ai-Ai for the latter extraction technique. This makes Ai-G a natural candidate for a portable interferometric benchmark of weak mean-field nonlinearities based on experimentally accessible observables.

For a systematics-aware theoretical uncertainty separated from statistical uncertainty and experimental systematics, the heteroskedasticity and autocorrelation consistent Newey-West estimator is applied. The reported uncertainty estimates can be interpreted as a practical lower bound on algorithmic systematics, indicating that comparable precision should be experimentally attainable.

In the previous analysis, the dynamics were reduced to an effective one-dimensional problem. In three dimensions, narrow Gaussian envelopes in the neglected directions should enable comparable collision geometries. It is worth reminding that the Kennard phase is not limited to the Airy profile, but emerges for arbitrary wave packets evolving in a linear potential. This is not restricted to ultracold atoms: any condensate platform governed to good approximation by effective Gross-Pitaevskii dynamics with an engineered potential gradient – including e.g. exciton-polariton [42, 43] or photonic Bose-Einstein condensate realizations [44] – should in principle exhibit the same cubic-in-time action phase and admit analogous interference-based phase reconstruction [12, 13].

⁵These intricacies could be dealt with by clever intermediate calibration, which would open the future realm to the strong interaction regime for Ai-Ai.

4.1. Experimental Outlook

Phase reconstruction via interference offers a direct pathway toward observing the Kennard phase of self-accelerating condensates in cold-atom experiments. By releasing a BEC prepared in an Airy-like state and overlapping it with a reference Gaussian cloud, one can image the interference fringes and extract the relative phase of the condensates. Such measurements would directly test the predicted cubic phase dynamics and provide an experimentally accessible observable that is sensitive to weak mean-field interactions. Tuning the interaction strength via Feshbach resonances would enable a calibrated test of the predicted response of the extracted cubic coefficient [45]. The realization could happen in free fall or in microgravity [46, 47]. Given the T^3 scaling of the Kennard phase, such interferometric access to the cubic term may also be relevant for precision acceleration measurements, provided that interaction-induced phase contributions are well calibrated [22, 27]. Furthermore, this experiment would extend interferometric observations of the Kennard phase to self-accelerating ultracold quantum fluids. In the longer term, the Ai-G collision could serve as a simple interference-based benchmark for weak mean-field nonlinearities via deviations of the extracted cubic coefficient. More broadly, the Kennard phase is tied to the action of a particle in a uniform force field [21], providing a clean phase observable for comparing accelerated-frame descriptions in matter-wave interferometry, and may therefore inform discussions of equivalence-principle tests in atom interferometry [48].

ACKNOWLEDGMENTS

We thank N. Schöneberg and K. D. Follmann for productive discussions. G.G.R. acknowledges additional support from the MIT School of Science Research Innovation Seed Fund.

CONTRIBUTIONS

Manuscript, simulations, and data analysis by M.P. Supervision and manuscript revision by G.G.R.

COMPETING INTERESTS

The authors declare no competing interests.

CORRESPONDENCE

Georgi Gary Rozenman: gary95@mit.edu

REFERENCES

- [1] K. B. Davis, M.-O. Mewes, M. R. Andrews, N. J. van Druten, D. S. Durfee, D. M. Kurn, and W. Ketterle. Bose-einstein condensation in a gas of sodium atoms. *Phys. Rev. Lett.*, 1995.
- [2] M. H. Anderson, J. R. Ensher, M. R. Matthews, C. E. Wieman, and E. A. Cornell. Observation of bose-einstein condensation in a dilute atomic vapor. *Science, New Series*, 1995.
- [3] F. Dalfovo, S. Giorgini, L. P. Pitaevskii, and S. Stringari. Theory of bose-einstein condensation in trapped gases. *Rev. Mod. Phys.*, 71:463–512, 1999.
- [4] A. J. Leggett. Bose-einstein condensation in the alkali gases: Some fundamental concepts. *Rev. Mod. Phys.*, 73:307–356, 2001.
- [5] C. J. Pethick and H. Smith. *Bose-Einstein Condensation in Dilute Gases*. Cambridge University Press, 2008.
- [6] L. P. Pitaevskii and S. Stringari. *Bose-Einstein Condensation*. Oxford University Press, 2003.
- [7] M. R. Andrews, C. G. Townsend, H. Miesner, D. S. Durfee, D. M. Kurn, and W. Ketterle. Observation of interference between two bose condensates. *Science*, 275(5300):637–641, January 1997.
- [8] M.-O. Mewes, M. R. Andrews, D. M. Kurn, D. S. Durfee, C. G. Townsend, and W. Ketterle. Output coupler for bose-einstein condensed atoms. *Phys. Rev. Lett.*, 78:582–585, 1997.
- [9] R. Carretero-González, D. J. Frantzeskakis, and P. G. Kevrekidis. Nonlinear waves in bose-einstein condensates: Physical relevance and mathematical techniques, 2008. arXiv:0805.0761.
- [10] I. Bloch, J. Dalibard, and W. Zwerger. Many-body physics with ultracold gases. *Rev. Mod. Phys.*, 80:885–964, 2008.
- [11] C. Barceló, S. Liberati, and M. Visser. Analogue gravity. *Living Rev. Relativ.*, 14(3), 2011.
- [12] H. Deng, H. Haug, and Y. Yamamoto. Exciton-polariton bose-einstein condensation. *Rev. Mod. Phys.*, 82(2):1489–1537, 2010.
- [13] I. Carusotto and C. Ciuti. Quantum fluids of light. *Rev. Mod. Phys.*, 85(1):299–366, 2013.
- [14] Y. Castin and R. Dum. Bose-einstein condensates in time dependent traps. *Phys. Rev. Lett.*, 77(27):5315–5319, December 1996.
- [15] Yu. Kagan, E. L. Surkov, and G. V. Shlyapnikov. Evolution of a bose-condensed gas under variations of the confining potential. *Phys. Rev. A*, 54(3):R1753–R1756, September 1996.
- [16] M. V. Berry and N. L. Balazs. Nonspreading wave packets. *Am. J. Phys.*, 1979.
- [17] G. A. Siviloglou and D. N. Christodoulides. Accelerating finite energy airy beams. *Optics Letters*, 32(8):979–981, 2007.
- [18] G. A. Siviloglou, J. Broky, A. Dogariu, and D. N. Christodoulides. Observation of accelerating airy beams. *Phys. Rev. Lett.*, 99(21):213901, 2007.
- [19] J. Broky, G. A. Siviloglou, A. Dogariu, and D. N. Christodoulides. Self-healing properties of optical airy beams. *Opt. Express*, 16(17):12880–12891, 2008.
- [20] N. Voloch-Bloch, Y. Lereah, Y. Lilach, A. Gover, and A. Arie. Generation of electron airy beams. *Nature*, 494(7437):331–335, 2013.
- [21] E. H. Kennard. Zur Quantenmechanik einfacher Bewegungstypen. *Zeitschrift für Physik*, 44:326–352, 1927.
- [22] M. Zimmermann, M. A. Efremov, A. Roura, W. P. Schleich, S. A. DeSavage, J. P. Davis, A. Srinivasan, F. A. Narducci, S. A. Werner, and E. M. Rasel. t^3 -interferometer for atoms. *Applied Physics B*, 123:102, 2017.
- [23] G. G. Rozenman, M. Zimmermann, M. A. Efremov, W. P. Schleich, L. Shemer, and A. Arie. Amplitude and phase of wave packets in a linear potential. *Phys. Rev. Lett.*, 122(12):124302, 2019.
- [24] L. D. Landau and E. M. Lifshitz. *Quantum Mechanics – Non-relativistic Theory*. Pergamon Press, 1965.
- [25] G. G. Rozenman, S. Fu, A. Arie, and L. Shemer. Quantum mechanical and optical analogies in surface gravity water waves. *Fluids*, 4:96, 2019.
- [26] G. G. Rozenman, M. Zimmermann, M. A. Efremov, W. P. Schleich, W. B. Case, D. M. Greenberger, L. Shemer, and A. Arie. Projectile motion of surface gravity water wave packets: An analogy to quantum mechanics. *The Eur. Phys. J. Spec. Top.*, 230:931–935, 2021. Published online: 16 April 2021.

- [27] O. Amit, Y. Margalit, J. Dobkowski, Z. Zhou, Y. Japha, M. Zimmermann, M. A. Efremov, F. A. Narducci, E. M. Rasel, W. P. Schleich, and R. Folman. t^3 stern-gerlach matter-wave interferometer. *Phys. Rev. Lett.*, 123(8):083601, 2019.
- [28] M. Raudonis, A. Roura, M. Meister, C. Lotz, L. Overmeyer, S. Herrmann, A. Gierse, C. Lämmerzahl, N. P. Bigelow, M. Lachmann, et al. Microgravity facilities for cold atom experiments. *Quantum Science and Technology*, 8(4):044001, 2023.
- [29] J. R. Williams, C. A. Sackett, H. Ahlers, et al. Pathfinder experiments with atom interferometry in the cold atom lab onboard the international space station. *Nat. Commun.*, 15:6414, 2024.
- [30] A. D. Cronin, J. Schmiedmayer, and D. E. Pritchard. Optics and interferometry with atoms and molecules. *Rev. Mod. Phys.*, 81(3):1051–1129, 2009.
- [31] J. Javanainen and J. Ruostekoski. Symbolic calculation in development of algorithms: Split-step methods for the gross-pitaevskii equation. *Journal of Physics A: Mathematical and General*, 39(12):L179–L184, 2006.
- [32] M. Olshanii. Atomic scattering in the presence of an external confinement and a gas of impenetrable bosons. *Phys. Rev. Lett.*, 81(5):938–941, 1998.
- [33] M. Abramowitz and I. A. Stegun. *Handbook of Mathematical Functions with Formulas, Graphs, and Mathematical Tables*, volume 55. US Government printing office, 1964.
- [34] W. P Schleich. *Quantum Optics in Phase Space*. Wiley-VCH, 2011.
- [35] R. P. Feynman and A. R. Hibbs. *Quantum Mechanics and Path Integrals*. Dover Publications, Mineola, 2010.
- [36] M. Takeda, H. Ina, and S. Kobayashi. Fourier-transform method of fringe-pattern analysis for computer-based topography and interferometry. *J. Opt. Soc. Am.*, 1982.
- [37] P. Cheinet, B. Canuel, F. P. Dos Santos, A. Gauguet, F. Yver-Leduc, and A. Landragin. Measurement of the sensitivity function in a time-domain atomic interferometer. *IEEE Transactions on Instrumentation and Measurement*, 57(6):1141–1148, 2008.
- [38] W. K. Newey and K. D. West. A simple, positive semi-definite, heteroskedasticity and autocorrelation consistent covariance matrix. *Econometrica*, 55(3):703–708, May 1987.
- [39] I. Bouchoule, N. J. van Druten, and C. I. Westbrook. Atom chips and one-dimensional Bose gases, 2009.
- [40] J. J. P. van Es, P. Wicke, A. H. van Amerongen, C. Rétif, S. Whitlock, and N. J. van Druten. Box traps on an atom chip for one-dimensional quantum gases, 2009.
- [41] N. P. Proukakis, J. Schmiedmayer, and H. T. C. Stoof. Quasi-condensate growth on an atom chip. *Phys. Rev. A*, 73(5):053603, 2006.
- [42] G. G. Rozenman, A. Peisakhov, and N. Zadok. Dispersion of organic exciton polaritons – a novel undergraduate experiment. *European Journal of Physics*, 43(3):035301, 2022.
- [43] G. G. Rozenman, K. Akulov, A. Golombek, and T. Schwartz. Long-range transport of organic exciton-polaritons revealed by ultrafast microscopy. *ACS Photonics*, 5(1):105–110, 2018.
- [44] J. Bloch, I. Carusotto, and M. Wouters. Non-equilibrium bose-einstein condensation in photonic systems. *Nature Reviews Physics*, 4(7):470–488, 2022.
- [45] C. Chin, R. Grimm, P. Julienne, and E. Tiesinga. Feshbach resonances in ultracold gases. *Reviews of Modern Physics*, 82(2):1225–1286, 2010.
- [46] D. Becker, M. D. Lachmann, S. T. Seidel, et al. Space-borne bose-einstein condensation for precision interferometry. *Nature*, 562(7727):391–395, 2018.
- [47] M. D. Lachmann, H. Ahlers, D. Becker, et al. Ultracold atom interferometry in space. *Nature Communications*, 12:1317, 2021.
- [48] G. Rosi et al. Quantum test of the equivalence principle for atoms in coherent superposition of internal energy states. *Nat. Commun.*, 8:15529, 2017.